MDPI

Article

Physical Simulation and Mathematical Model of the Porous Flow Characteristics of Gas-Bearing Tight Oil Reservoirs

Yuan Rao [1,2], **Zhengming Yang** [2,3], **Yapu Zhang** [2,3], **Zhenkai Wu** [1,2,*], **Yutian Luo** [2,3], **Haibo Li** [2,3] **and Ying He** [2,3]

[1] College of Engineering Science, University of Chinese Academy of Sciences, Beijing 100049, China; raoyuan171@mails.ucas.edu.cn

[2] Institute of Porous Flow and Fluid Mechanics, University of Chinese Academy of Sciences, Langfang 065007, China; yzhm69@petrochina.com.cn (Z.Y.); zhangyapu69@petrochina.com.cn (Y.Z.); luoyutian@petrochina.com.cn (Y.L.); Lihaibo05@petrochina.com.cn (H.L.); heying69@petrochina.com.cn (Y.H.)

[3] Research Institute of Petroleum Exploration and Development, Beijing 100083, China

* Correspondence: wuzhenkai17@mails.ucas.edu.cn

Abstract: The separation of solution gas has great influence on the development of gas-bearing tight oil reservoirs. In this study, physical simulation and high-pressure mercury intrusion were used to establish a method for determining the porous flow resistance gradient of gas-bearing tight oil reservoirs. A mathematical model suitable for injection–production well networks is established based on the streamline integral method. The concept of pseudo-bubble point pressure is proposed. The experimental results show that as the back pressure decreases from above the bubble point pressure to below the bubble point pressure, the solution gas separates out. During this process, the porous flow resistance gradient is initially equal to the threshold pressure gradient of the oil single-phase fluid, then it becomes relatively small and stable, and finally it increases rapidly and exponentially. The lower the permeability, the higher the pseudo-bubble point pressure, and the higher the resistance gradient under the same back pressure. For tight reservoirs, the production pressure should be maintained above the pseudo-bubble point pressure when the permeability is lower than a certain value. When the permeability is higher than a certain value, the pressure can be reduced below the pseudo-bubble point pressure, and there is a reasonable range. The mathematical results show that after degassing, the oil production rate and the effective utilization coefficient of oil wells decline rapidly. These declines occur later and have a flat trend for high permeability formations, and the production well pressure can be reduced to a lower level. Fracturing can effectively increase the oil production rate after degassing. A formation that cannot be utilized before fracturing because of the blocked throats due to the separation of the solution gas can also be utilized after fracturing. When the production well pressure is lower than the bubble point pressure, which is not too large, the fracturing effect is better.

Keywords: gas-bearing tight oil; resistance gradient; high-pressure mercury intrusion; microscopic; productivity prediction

1. Introduction

With the continuous growth of the global oil and gas demand and the continuous decline of conventional oil and gas production, unconventional oil and gas resources are increasingly being valued by various countries and oil companies. Unconventional oil and gas resources include heavy oil, tight oil, shale oil and gas, coalbed methane and natural gas hydrates. As a typical unconventional petroleum resource, tight oil is a research focus of exploration and development [1–5]. China has a wide distribution and diversity of tight oil, which is an important renewable resource. The recoverable tight oil reserves are predicted to be about $(20–25) \times 10^8$ t [6–9]. Tight oil is light in quality, often bearing solution gas, and the original gas–oil ratio in some tight oil fields is high. In heavy oil

reservoirs, asphaltene particles are very problematic. However, in light oil reservoirs, there is less of a risk of asphaltene deposition. Asphaltene deposition is one of the most serious problems in the industry at the moment and it significantly increases the expenses. Many scholars have carried out particle-scale modeling studies on the problem of asphaltene deposition [10–12]. The tight sandstone of the Yanchang Formation in the Ordos Basin and the tight sandstone and limestone of the Jurassic strata in central Sichuan are the most typical. Due to the narrow pore throats of tight formations, it is difficult to supplement the formation energy, so development is usually by natural depletion, which leads to a rapid decrease in the formation pressure. When the pressure drops to the bubble point pressure, the solution gas separates out, resulting in a sharp decline in production, which seriously affects the efficiency of tight oil development [13–15]. Therefore, it is of great importance to conduct research on porous flow resistance to effectively develop gas-bearing tight oil reservoirs. At present, few studies have been conducted on porous flow resistance in gas-bearing tight oil reservoirs in China and abroad [16,17], and more studies have focused on heavy oil and medium-high permeability reservoirs. For heavy oil reservoirs, Akin and Kovscek and other scholars have used the visualization method to study the influence of solution gas separation on heavy oil flow [18–23]. Cui and other scholars have studied the flow performance of heavy oil after the solution gas separates from the oil [24–28]. They have also analyzed the factors influencing the oil flow properties, such as the solution gas–oil ratio, the pressure depletion rate, and the pore throat size. These studies mainly focused on the microscopic porous flow mechanism, but they did not involve porous flow resistance. For medium-high permeability reservoirs, the porous flow resistance is low when a small amount of solution gas separates out because of the large pore throats, so the production pressure can be reduced to from 20% to 30% below the bubble point pressure [29–32]. However, whether the research results for medium-high permeability reservoirs can be applied to tight reservoirs requires further study. Many scholars have established empirical and theoretical models suitable for the two-phase flow of oil and gas in gas-bearing reservoirs and have calculated the formation pressure distribution, degassing radius, production rate, and minimum allowable pressure of oil wells [33–38], but the calculation process is mostly cumbersome. In this paper, a physical simulation experiment and the high-pressure mercury intrusion method were used to analyze the structural characteristics of micropores with different permeabilities. A test method for porous flow resistance in gas-bearing tight oil reservoirs was established. The effects of the different cores and gases on the production of gas-bearing tight oil reservoirs were studied. Based on the streamline integral method, equations for calculating the production rate and the effective utilization coefficient that are suitable for injection–production well networks were derived and the influencing factors were analyzed.

2. Experiments

2.1. Materials

The three tight sandstone cores used in the experiments were collected from the Yanchang Formation in the Ordos Basin. The parameters of the cores were presented in Table 1. The oil used in the experiments was degassed crude oil from the Yanchang Formation. The gas-bearing oil was compounded in a PVT apparatus set according to the main components of the gas associated with the on-site crude oil (Table 2).

Table 1. Parameters of the three cores.

Number	Length (cm)	Diameter (cm)	Porosity (%)	Gas Log Permeability (mD)
16-1B	4.29	2.49	11.25	0.12
11-4A	4.16	2.51	10.48	0.29
97	6.21	2.50	13.23	0.53

Table 2. Components of the gas associated with the crude oil.

Components	Mole Fraction (%)
CH_4	54.8
C_2H_6	37.0
C_3H_8	5.0
N_2	3.2

The compound formation water used in the experiments was prepared according to the main components of the formation water of the Yanchang Formation (Table 3). The other parameters of the experiments were determined according to the reservoir parameters of the Yanchang Formation (Table 4). The bubble point pressure test of the compound gas-bearing oil was carried out before the experiment. The result is shown in Figure 1. The bubble point pressure of the gas-bearing oil was 10.72 MPa under the formation conditions.

Table 3. Components of the compound formation water.

Distilled Water (L)	NaCl (g)	CaCl$_2$ (g)	MgCl$_2$ (g)
1	43.75	3.75	2.50

Table 4. Parameters of the experiments.

Solution Gas–Oil Ratio (m^3/t)	Viscosity of Degassed Oil (mPa·s)	Viscosity of Formation Oil (mPa·s)	Temperature (°C)	Formation Pressure (MPa)	Bubble Point Measured in PVT Apparatus Set (MPa)
80	4.3	1.23	72	18	10.72
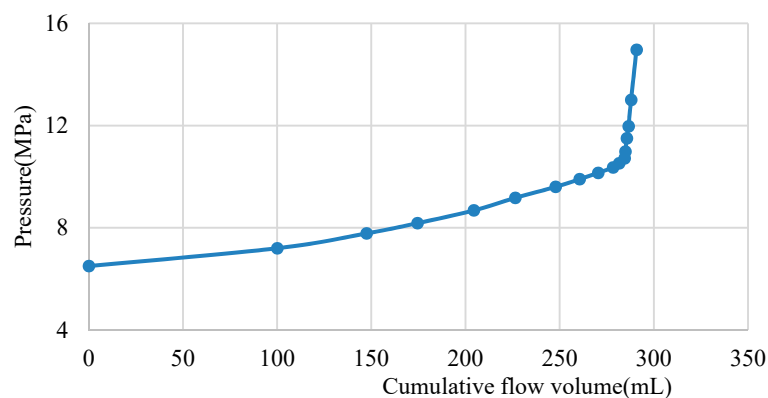
Figure 1. Bubble point pressure test curve.

2.2. Methods

2.2.1. Microscopic Structural Characteristics

The size and distribution of the pore throats are important factors affecting the porous flow capacity of tight sandstone reservoirs [39–42]. A high-pressure mercury intrusion porosimeter was used to analyze the microscopic structural characteristics of the pore throats.

The high-pressure mercury intrusion technique is based on the capillary model and uses a non-wetting phase to displace the wetting phase. The capillary pressure curve and pore throat distribution curve can be obtained by continuously changing the injection pressure. The minimum pore size that can be tested using a high-pressure mercury intrusion porosimeter is 2 nm [43].

A PoreMaster® 60/33 mercury intrusion porosimeter (Quantachrome Company, 1900 Corporate Drive, Boynton Beach, FL, USA) was used in the experiments. The samples tested were three small columnar cores. The oil in the cores was washed out before the

mercury injection experiments, and the cores were dried at 105 °C to a constant weight. The mercury intrusion experiment included pressurizing mercury injection and depressurizing mercury withdrawal. The highest experimental pressure was 340 MPa.

2.2.2. Porous Flow Resistance Test

In tight oil reservoirs, when the production pressure is higher than the bubble point pressure, the solution gas in the crude oil was not separated out. This stage is in single-phase nonlinear porous flow, which mainly relies on the elastic energy of the oil, and the resistance gradient is mainly caused by the oil phase alone [44]. When the pressure is lower than the bubble point pressure, the solution gas separates out. The oil and gas two-phase porous flow first occurs near the bottom of the well, and then it expands further into the formation. Then, a resistance gradient forms as a result of the oil phase and the Jamin effect generated by the gas phase. The Jamin effect is the resistance generated when the gas passes through the throats (Figure 2). The smaller the radius of the throats, the greater the resistance.
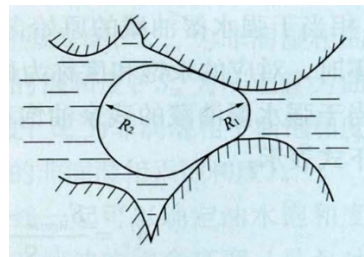
Figure 2. A sketch of the Jamin effect.

In order to quantitatively characterize the porous flow resistance of the gas-bearing tight oil in the experiment, a coefficient was defined. The ratio of the pressure difference between the two ends of the core to the core's length was defined as the resistance coefficient R:

$$R = \frac{p_{in} - p_{out}}{L} \tag{1}$$

where R is the resistance gradient; p_{in} is the final stable pressure at the core inlet; p_{out} is the back pressure at the core outlet; and L is the core's length.

The experimental process is shown in Figure 3. It consists of three systems: a gas-bearing oil blending system, a displacing system, and a back pressure controlling system. The gas-bearing oil blending system includes a TC-100D constant speed pressure pump, a PVT apparatus, and an intermediate container filled with kerosene. The displacing system includes a core holder, a confining pressure pump, inlet and outlet pressure sensors, a differential pressure transducer with an accuracy of 0.0015 MPa, a computer, and recording software. The back pressure controlling system includes a piston-equipped container and a nitrogen constant pressure pump. All cores were aged and saturated with compound formation water for three days before the experiment. The experiment was carried out in a constant temperature system.

The experimental steps are as follows. ① Connect the equipment according to Figure 3, and use the constant speed pressure pump to raise the pressure in the back pressure intermediate container to 16 MPa. ② Use kerosene to displace the fluid in the core holder and the pipeline without applying a confining pressure. Then, raise the pressure in the pipeline at both ends of the core holder to 17.5 MPa. ③ Apply a confining pressure of 20 MPa; open the valves between the core holder and the back pressure intermediate container; and use the prepared gas-bearing oil to displace the core under a constant pressure of 18 MPa. After displacing the pore volume 10 times, close the valves. ④ Open the valve of the differential pressure transducer and use the computer software to record the sensor reading every 1 min until the change in the pressure difference is less than 0.15% in an hour. ⑤ Reduce the pressure in the back pressure intermediate container regularly,

and repeat step 4 to obtain a stable pressure difference between the core at the different back pressures. Calculate the resistance gradient coefficient *R* using Equation (1).
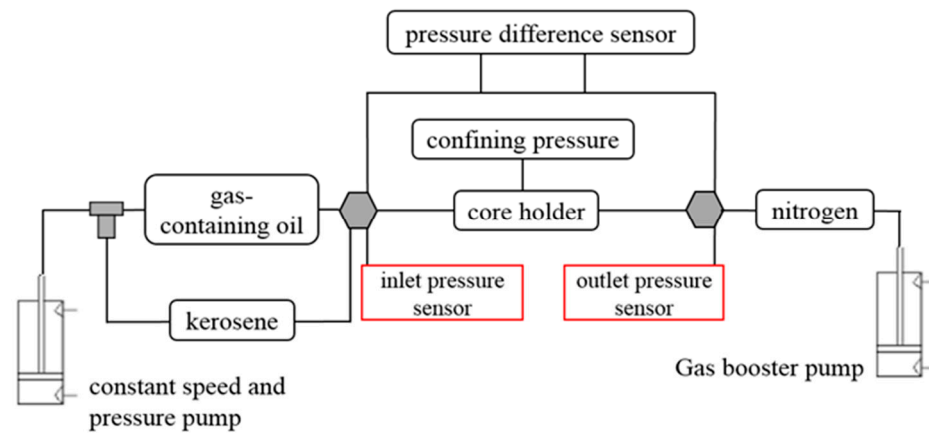
Figure 3. Flowchart of the resistance gradient experiment.

2.3. Results

2.3.1. Microscopic Structural Characteristics of the Pore Throats

The high-pressure mercury intrusion curves of the three cores are shown in Figure 4. Core 16-1B has the highest median pressure (5.7 MPa) and displacement pressure (3.1 MPa). Cores 11-4A and 97 have lower pressures of 2.8 MPa and 0.8 MPa and 2.3 MPa and 0.4 MPa, respectively (Table 5). This demonstrates that core 16-1B has relatively narrow throats, with a median radius of 0.1289 μm, while core 11-4A and core 97 have wider throats, with median radii of 0.2542 μm and 0.3067 μm, respectively.
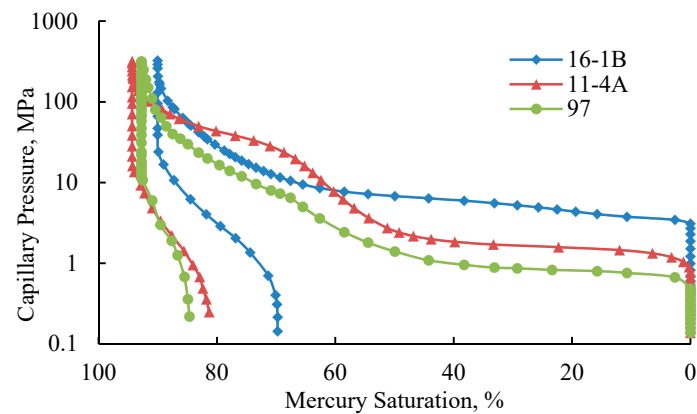
Figure 4. HPMI curves of the three cores.

Table 5. HPMI results for the three cores.

Number	Median Radius (μm)	Median Pressure (MPa)	Displacement Pressure (MPa)
16-1B	0.1289	5.7	3.1
11-4A	0.2542	2.8	0.8
97	0.3067	2.3	0.4

According to the experimental results, the pore volume percentage and permeability contribution rate were calculated (Figure 5). The radii of the throats that mainly contribute to the permeability of core 16-1B mainly range from 0.05 to 0.30 μm, and the peak value of the permeability contribution curve is located at a throat radius of 0.18 μm. The radii of the

throats that mainly contribute to the permeability of core 11-4A mainly range from 0.15 to 0.70 μm, and the peak value of the permeability contribution curve is located at a throat radius of 0.34 μm. The radii of the throats that mainly contribute to the permeability of core 97 mainly ranging from 0.15 to 0.80 μm, and the peak value of the permeability contribution curve is located at a throat radius of 0.39 μm. Thus, as the permeability increases, the number of wider throats increases, and the curves gradually move toward the right.

(**a**) **Core 16-1B.**

(**b**) **Core 11-4A.**

(**c**) **Core 97**
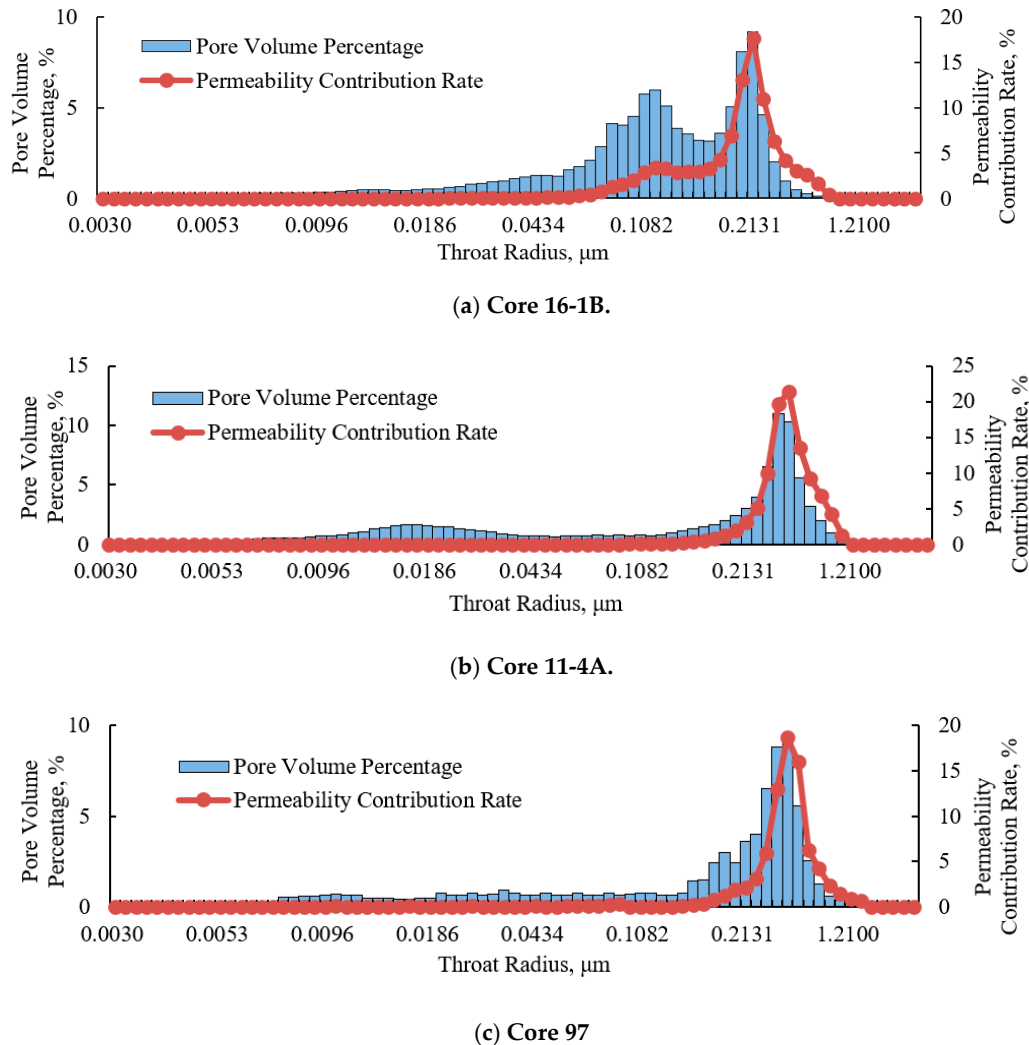
Figure 5. Pore throat distribution frequencies and permeability contributions of the three cores.

2.3.2. Porous Flow Resistance

The porous flow resistance gradient under different back pressures was calculated according to the equation that defines the resistance gradient. The relationship between the back pressure and the resistance gradient of the three cores is shown in Figure 6. As can be seen:

(1) When the back pressure is higher than the bubble point pressure, the solution gas in the crude oil did not separate out. At this time, the porous flow resistance was the threshold pressure gradient, and the curve was relatively smooth (section a). At a certain value below the bubble point pressure, the solution gas begins to separate out, and the porous flow resistance increases, so the curve rises gradually (section b). When the back pressure is decreased further, the solution gas forms a continuous gas phase, resulting in

a rapid increase in the resistance gradient, and the curve grows exponentially (section c). Taking core 16-1B as an example, the exponential relationship is:

$$R = 352642.05p^{-6.28} \tag{2}$$
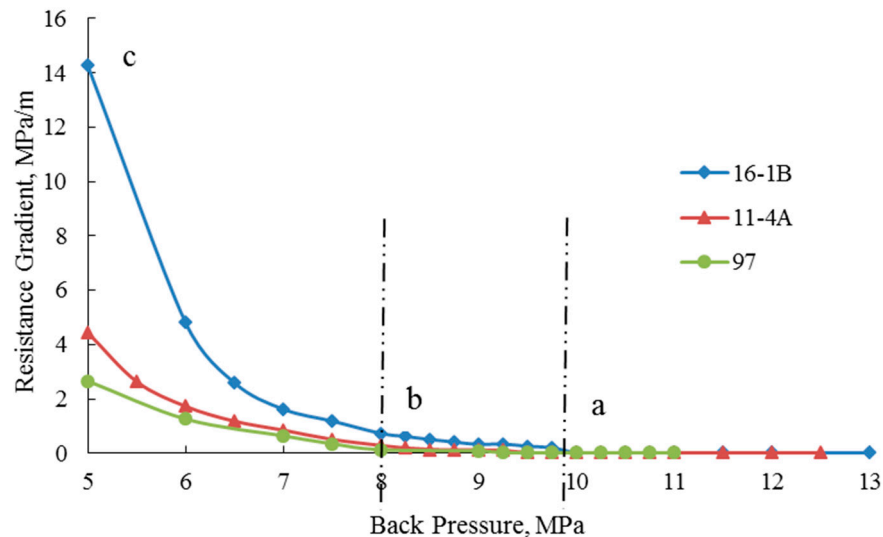
Figure 6. Relationship between the back pressure and the porous flow resistance gradient.

(2) When the back pressure is lower than the bubble point pressure (10.72 MPa), the solution gas in the three cores has not separated out. Only when the pressure is lower than a certain value below the bubble point will the solution gas begin to separate out and cause resistance. In this study, the pressure at which the resistance gradient begins to form due to the separation of the solution gas is defined as the pseudo-bubble point pressure. The pseudo-bubble point pressures of cores 16-1B, 11-4A, and 97 are 9.75 MPa, 9.25 MPa, and 9.00 MPa, respectively, which are all lower than the bubble point pressure (10.72 MPa) measured using the PVT apparatus (Table 6). This result is consistent with the theoretical analysis results [45–48], that the PVT characteristic in the nanopores is different to that measured using the PVT apparatus. The lower the permeability, the higher the pseudo-bubble point pressure, and the higher the pressure at which the resistance caused by the solution gas occurs.

Table 6. Pseudo-bubble point pressures and corresponding resistance gradients of the three cores.

Number	Gas Log Permeability (mD)	Pseudo-Bubble Point Pressure (MPa)	Resistance Gradient Under Pseudo-Bubble Point Pressure (MPa/m)
16-1B	0.12	9.75	0.482
11-4A	0.30	9.25	0.106
97	0.53	9.00	0.085

(3) For the same back pressure, the smaller the permeability, the greater the resistance gradient. As shown in Table 5, when the back pressure was 9.75 MPa, the resistance gradient of core 16-1B was 0.202 MPa/m, and those of cores, 11-4A and 97 were both 0.020 MPa/m. When the back pressure was 8 MPa, the resistance gradient of core 16-1B was 0.532 MPa/m, whilst that of core 11-4A was 0.115 MPa/m, and that of core 97 was 0.093 MPa/m. This is because bubble nucleation and growth occur when the back pressure is lower than the bubble point pressure. When the permeability is low, the newly formed tiny bubbles will produce porous flow resistance because the throats are narrow. When the permeability is high, the tiny bubbles will not produce a resistance gradient because

the throats are wide. According to the Jamin effect, the resistance gradient is different when bubbles of the same size pass through throats of different sizes. The smaller the radii of the throats, the greater the resistance. Combined with the results of the high-pressure mercury intrusion experiments, cores 11-4A and 97 have wider throats and similar pore throat structures, while core 16-1B has relatively narrow throats. Thus, core 16-1B has the greatest resistance gradient, while those of the other two cores are smaller and are similar.

As can also be seen from the above discussion, if a core is tighter, the pseudo-bubble point pressure will be higher, and the resistance caused by the separation of the solution gas will be greater. Thus, in the development of gas-bearing tight oil reservoirs, the lower the permeability, the smaller the interval of the production pressure difference.

Solution gas separation can be divided into three stages: an elastic-driven stage without separated solution gas, a transition stage with a small amount of separated solution gas, and a blocking stage with a large amount of separated solution gas [23]. In the elastic driven stage, there is oil single-phase flow and the oil and gas are in a supersaturated state. In the transition stage, the solution gas begins to separate out, which is a dynamic equilibrium process in which bubbles break up and coalesce. In the blocking stage, the pressure continues to drop and a large amount of solution gas separates out. A large number of bubbles separate out and coalesce, forming oil and gas two-phase flow and blocking the porous flow passages. The stable part of the resistance gradient curve corresponds to the elastic-driven stage and the transition stage, in which the back pressure begins to decrease below the bubble point pressure. In this stage, the solution gas begins to separate out, but it does not yet form a continuous gas phase. The separated gas provides part of the elastic energy, which keeps the resistance gradient relatively stable. This stage is favorable for development and should be used to control the pressure in order to maintain the production capacity. According to the experimental results, the resistance of core 16-1B is still large in the stable part of the curve, and thus, it cannot be exploited under natural depletion conditions. While the resistances of cores 11-4A and 97 are not that large in the stable parts of the curves, and the production pressure can be reduced to 8 MPa (about 15% below the bubble point pressure). Thus, for tight oil reservoirs, when the permeability is less than a certain value (0.3 mD), the production pressure should be maintained above the pseudo-bubble point pressure (about 10% below the bubble point pressure). When the permeability is greater than a certain value (0.3 mD), the production pressure can be lowered to below the pseudo-bubble point pressure (about 15% below the bubble point pressure).

3. Mathematical Model of Gas-Bearing Tight Oil

Injection wells are often used in oilfields to supplement the energy required for development. When the pressure of the production wells is lower than the bubble point pressure, the solution gas will separate out. When the gas passes through the throats, additional porous flow resistance will be generated due to the Jamin effect, which will affect the productivity. The current numerical simulation methods for the development of gas-bearing tight oil reservoirs are very cumbersome, so it is necessary to establish a set of simple and practical calculation methods.

3.1. Physical Model and Assumptions

The streamline integral method is a commonly used calculation method in the field of fluid mechanics. The streamline is the route that the fluid particles follow from the injection wells to the production wells. The area bordered by two streamlines is called the stream tube (Figure 7). Flow tubes have the following properties. Flow tubes cannot intersect; the shape and position of flow tubes do not change with time during steady state flow; and flow tubes cannot be broken off inside the flow field. The flow field is divided into infinite stream tubes with the streamline as the boundary. The flow of the fluid in the formation can be regarded as the flow of fluid from the injection wells to the production wells along

these tiny stream tubes. The total output of the production well is equal to the sum of the productions of all of the stream tubes directed to the well [49].
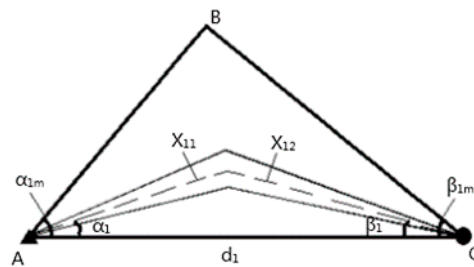
Figure 7. Sketch of a stream tube.

Assumptions:

1. Oil and gas two-phase porous flow;
2. The threshold pressure gradient of the oil phase is considered;
3. The compressibility of the oil and gas is considered;
4. Gas can dissolve in or separate from the oil;
5. The compressibility of the rock is negligible, and the porosity is regarded as being constant;
6. The porous flow process is steady state and isothermal.

3.2. Mathematical Model

This paper takes a five-point well network as an example to derive the single well production rate and the effective utilization coefficient before and after fracturing (Figure 8).
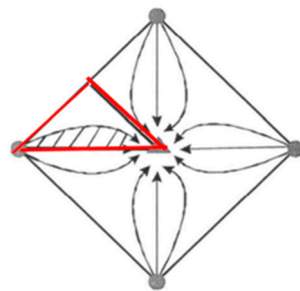
Figure 8. Five-point well network.

Assuming that there are a series of stream tubes among the oil and water wells, based on Darcy's law of oil and gas, two-phase stable porous flow and considering the threshold pressure gradient and the additional resistance gradient generated when the solution gas separates out, the rate of the flow at the cross-section is:

$$\Delta q_o = \frac{k k_{ro} A(\varepsilon)}{B_o(p) \mu_o(p)(1 + R_{resis})} \left(\frac{dp}{d\varepsilon} - \lambda \right) \tag{3}$$

For an injection–production well unit, the radius of the well is r_w; the distance between the wells is d; the centerline of the stream tube is composed of X_{11} and X_{12}; the angle increments are $\Delta\alpha$ and $\Delta\beta$; and ω is the length coefficient.

Derived from elementary geometry:

$$X_1 = \frac{\omega d \sin \beta}{\sin(\alpha + \beta)} \tag{4}$$

$$X_2 = \frac{\omega d \sin \alpha}{\sin(\alpha + \beta)} \tag{5}$$

Since $\Delta\alpha$ and $\Delta\beta$ are infinitely small, the cross-sectional area of the stream tube can be approximated as follows:

$$A_1(\xi) = 2h\xi_1 \text{tg} \frac{\Delta\alpha}{2} \tag{6}$$

$$A_2(\xi) = 2h\xi_2 \text{tg} \frac{\Delta\beta}{2} \tag{7}$$

$$r_w \leq \xi_1 \leq X_1 = \frac{\omega d \sin\beta}{\sin(\alpha+\beta)} \tag{8}$$

$$r_w \leq \xi_2 \leq X_2 = \frac{\omega d \sin\alpha}{\sin(\alpha+\beta)} \tag{9}$$

Based on the geometric relationship:

$$\Delta\alpha = \Delta\beta \tag{10}$$

The yield equation can be obtained from the above equation:

$$\Delta q_o = \frac{k \int_{p_w}^{p_e} \frac{k_{ro}(S)}{B_o(p)\mu_o(p)[1+R_{resis}(p)]}dp - \lambda\omega d\frac{\sin\alpha+\sin\beta}{\sin(\alpha+\beta)}}{\int_{r_w}^{X_1}\frac{d\varepsilon}{2h\varepsilon_1 \tan\frac{\Delta\alpha}{2}} + \int_{r_w}^{X_2}\frac{d\varepsilon}{2h\varepsilon_2 \tan\frac{\Delta\beta}{2}}} \tag{11}$$

The pressure function H can be defined as

$$H = \int \frac{k_{ro}(S)}{B_o(p)\mu_o(p)[1+R_{resis}(p)]}dp + C \tag{12}$$

R_{resis} is the fitting result of the experimental curve of the porous flow resistance gradient (Figure 9).
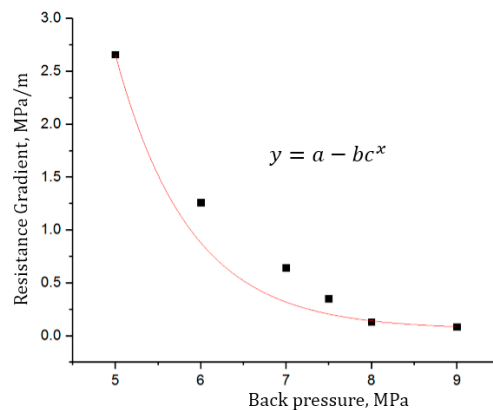
Figure 9. Schematic diagram of fitting results.

According to Equations (11) and (12), the single well production rate of the injection–production unit is:

$$q_o = \int_0^{\alpha_0} \frac{kh\left[(H_e - H_w) - \lambda\omega d\frac{\sin\alpha+\sin\beta}{\sin(\alpha+\beta)}\right]}{\ln\frac{\omega d \sin\beta}{r_w \sin(\alpha+\beta)} + \frac{\alpha_m}{\beta_m}\ln\frac{\omega d \sin\alpha}{r_w \sin(\alpha+\beta)}}d\alpha \tag{13}$$

$$\alpha_m = \beta_m = \frac{\pi}{4} \tag{14}$$

$$\alpha = \beta \tag{15}$$

$$\Delta\alpha = \Delta\beta \tag{16}$$

where q_o is the rate of flow; k is the permeability; h is the formation thickness; μ is the viscosity of the formation fluid; p_e is the injection well pressure; p_w is the production well pressure; λ is the threshold pressure gradient of the oil phase; d is the well spacing; α is the injection well angle; β is the production well angle; α_m and β_m are the angles of the calculation unit; and r_w is the well radius.

Notice that $H_e - H_w$ is the key to the problem. $B_o(p)$ and $\mu_o(p)$ can be obtained from a high-pressure physical property experiment. k_{ro} should be obtained based on the assumption that the production gas–oil ratio R is a constant. Thus, we can obtain k_{rg}/k_{ro} and the saturation at any pressure, and the $\frac{k_{ro}}{B_o \mu_o [1+R_{resis}]} - p$ curve can be drawn. According to the geometric meaning of the definite integral, $H_e - H_w$ can be calculated. The denominator on the right side of Equation (13) is always greater than zero. When the numerator is zero, the single well production generated by the injection–production pressure difference was zero. Due to the existence of threshold pressure gradient and the solution gas resistance, not all of the area can be put to use under a certain injection–production pressure difference. The ratio of the area covered by the injection well to the area of the entire unit is the effective utilization coefficient, which is an important index for measuring the degree of reservoir utilization (Figure 10).
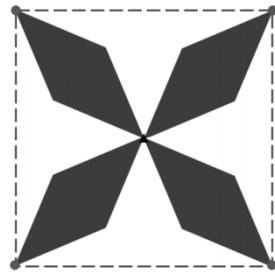
Figure 10. Diagram of the effective utilization factor.

When the single well production is zero, the maximum available injection well and production well angles α_0 and β_0 can be obtained using the following equation:

$$H_e - H_w - \lambda \omega d \frac{\sin \alpha + \sin \beta}{\sin(\alpha + \beta)} = 0 \tag{17}$$

It is considered that $\alpha_0 \leq \alpha_m$, so the upper limit of the integral of Equation (14) is:

$$\alpha = \min\{\alpha_0, \alpha_m\} \tag{18}$$

The single well output of the rectangular well network is:

$$Q_o = 8q_o \tag{19}$$

The effective utilization coefficient is:

$$eff = \tan \alpha \tag{20}$$

The above is the calculation of the production rate and effective utilization coefficient without considering fracturing. When considering fracturing, first use a quarter of one well network for the partition calculation. The principle of the partition is to keep the partition unit consistent with the actual streamline situation. Based on this, a quarter of the well network is divided into three parts (Figures 11 and 12).
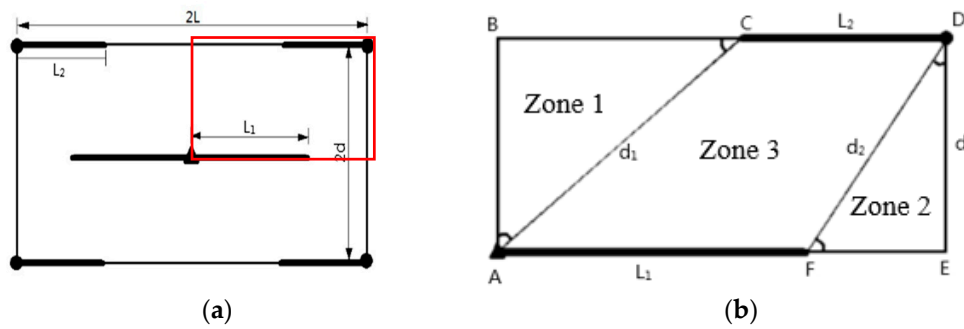
Figure 11. Rectangular well network after fracturing: (**a**) the entire well network; (**b**) the partition of a quarter of the well network.
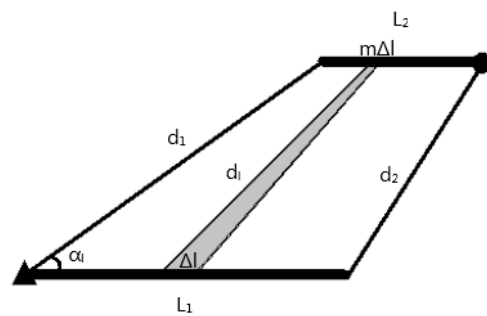
Figure 12. Schematic diagram of the Zone 3 computation unit.

For Zone 1 and Zone 2, the calculation method is the same as that before fracturing. For Zone 3, the equation for calculating the production rate is:

$$q_{\mathrm{III}} = \int_0^l \frac{kh(H_{w2} - H_{w1} - \lambda d_l)}{\frac{\ln m}{m-1} d_l} dl \tag{21}$$

By substituting the required physical property parameter conditions (as shown in Figure 13), the production rate and effective utilization coefficient can be calculated.
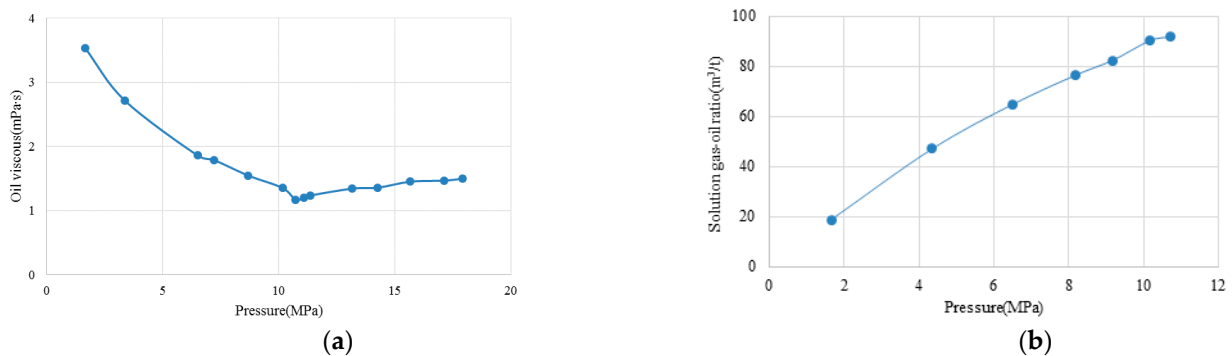
Figure 13. Some of the required physical property parameter conditions: (**a**) crude oil viscosity-pressure; (**b**) solution gas–oil ratio pressure.

3.3. Results and Discussion

Taking a rectangular well network as an example, when the permeabilities are 0.12 mD, 0.30 mD, and 0.53 mD; the distance between the injection and production wells is 150 m; the injection well pressure is 25 MPa; the bubble point pressure is 10.7 MPa; the reservoir thickness is 5 m; $\mu = 1.23$ mPa·s; the calculation results are as follows.

3.3.1. Influence of Production Well Pressure

As can be seen from Figures 14 and 15, before degassing, the production rate of the oil wells basically increases linearly as the production well pressure decreases; and the higher the permeability, the greater the production rate. After degassing, the production rate decreases rapidly. The degassing process is relatively late, with a higher permeability; the decrease in the production rate is relatively gentle, and the production pressure can be reduced to a lower level. After fracturing, under the same conditions, the decrease in production after degassing is gentler than that before fracturing, and the production pressure can be reduced to a lower level.
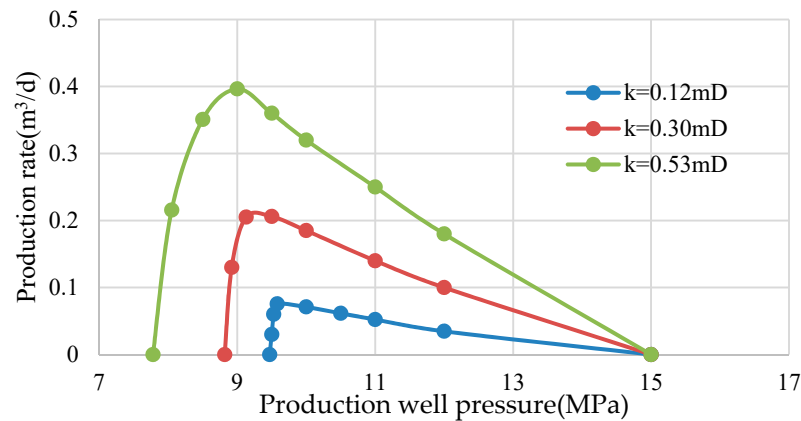
Figure 14. The relationship between the production rate and the production well pressure before fracturing.
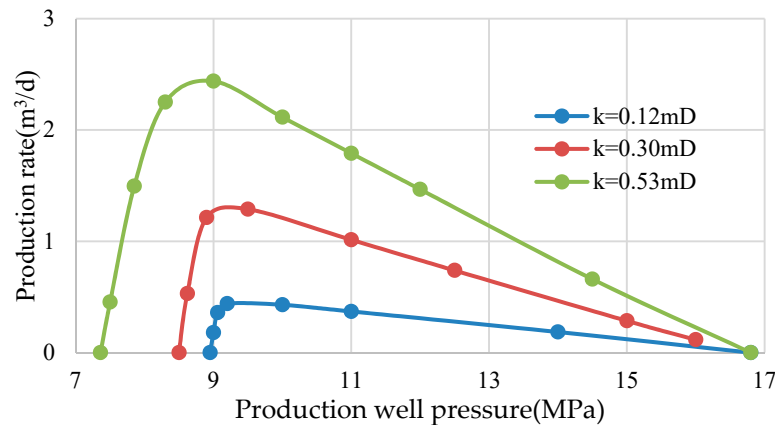
Figure 15. The relationship between the production rate and the production well pressure after fracturing.

When the pressure of the production well drops below the bubble point pressure, the solution gas separates out, and the effective utilization coefficient initially decreases slowly and then decreases rapidly. The lower the permeability, the steeper the downward trend. Under the same pressure, the effective utilization coefficient is larger after fracturing than before fracturing; and the lower the permeability, the greater the increase (Figures 16 and 17).
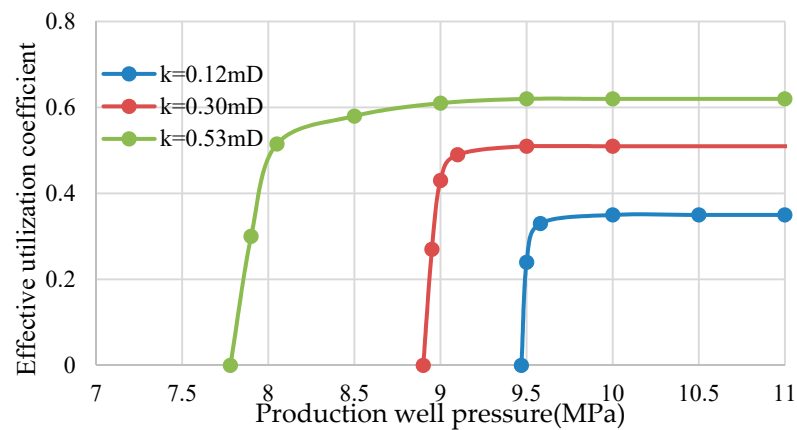
Figure 16. The relationship between the effective utilization coefficient and the production well pressure before fracturing.
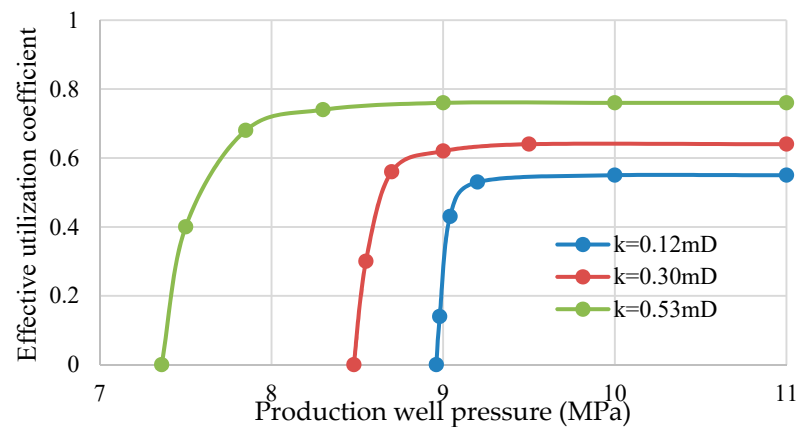
Figure 17. The relationship between the effective utilization coefficient and the production well pressure after fracturing.

3.3.2. The Impact of Well Spacing

As can be seen from Figure 18, before degassing, as the production well pressure decreases, the well production increases; and the higher the permeability, the greater the increase. After degassing, the well production decreases with decreasing pressure. When the permeability is high, the decrease is smaller; and when the permeability is low, the decrease is greater. This indicates that a formation with a low permeability has narrower throats, and even tiny bubbles can cause a great deal of resistance, so degassing should be avoided during development.

After fracturing, the production rate under the same conditions increases significantly, and the suitable well spacing increases significantly. Fracturing can effectively increase the output after degassing. A formation that cannot be utilized before fracturing because the throats were blocked by the separated gas can also produce some output. When the production well pressure is not much lower than the bubble point pressure, the fracturing effect is better (Figure 19).

As the well spacing increases, the effective utilization coefficient initially remains steady and then gradually decreases. Before degassing, the lower the production well pressure, the later the effective utilization coefficient decreases, and the larger the suitable well spacing. After degassing, the effective utilization coefficient decreases earlier, and the suitable well spacing decreases. Under the same conditions, the effective utilization coefficient of the formation with the high permeability is larger, and it is less affected by the production well pressure after degassing (Figure 20).

(**a**) k = 0.12 mD   (**b**) k = 0.30 mD   (**c**) k = 0.53 mD
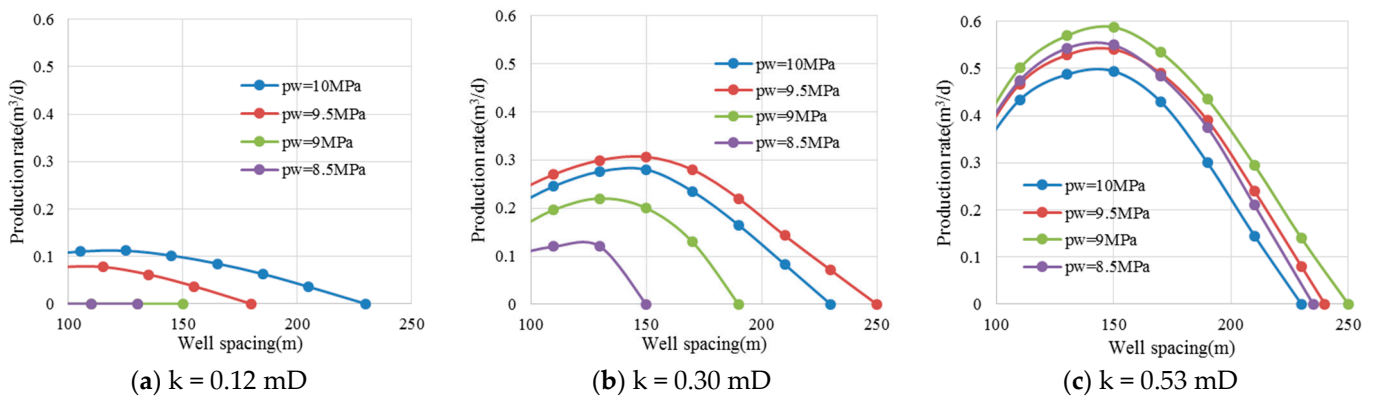
Figure 18. The relationship between the production rate and the well spacing before fracturing.

(**a**) k = 0.12 mD   (**b**) k = 0.30 mD   (**c**) k = 0.53 mD
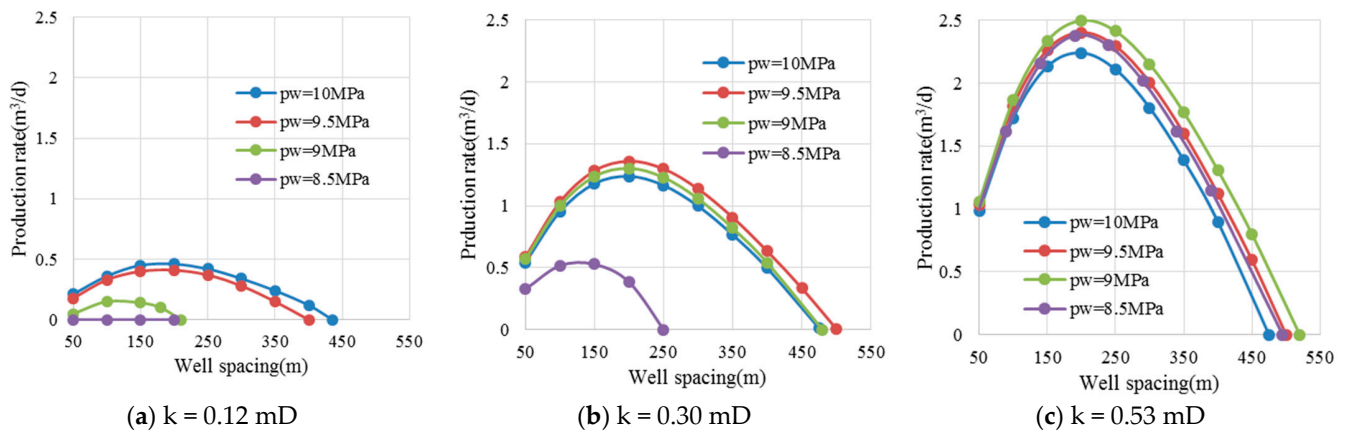
Figure 19. The relationship between the production rate and the well spacing after fracturing.

(**a**) k = 0.12 mD   (**b**) k = 0.30 mD   (**c**) k = 0.53 mD
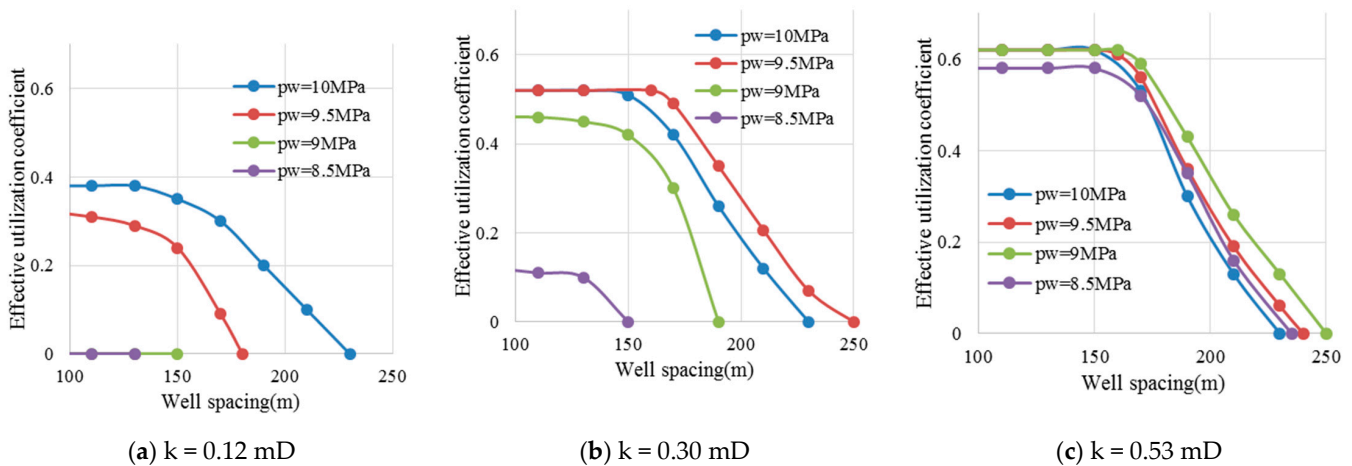
Figure 20. The relationship between the effective utilization coefficient and the well spacing before fracturing.

After fracturing, as the well spacing increases, the effective utilization coefficient initially decreases slowly, and then it rapidly decreases after reaching a certain well spacing. To make the reservoir well produce, the well spacing should be selected before the inflection point, and it should be closer to the highest value. After fracturing, under the same conditions, the effective utilization coefficient is significantly increased compared with that before fracturing. A formation that could not be utilized because the throats were blocked by the separated gas can also be effectively utilized. When the production well pressure is

lower than the bubble point pressure, which is not too large, the fracturing effect is better (Figure 21).
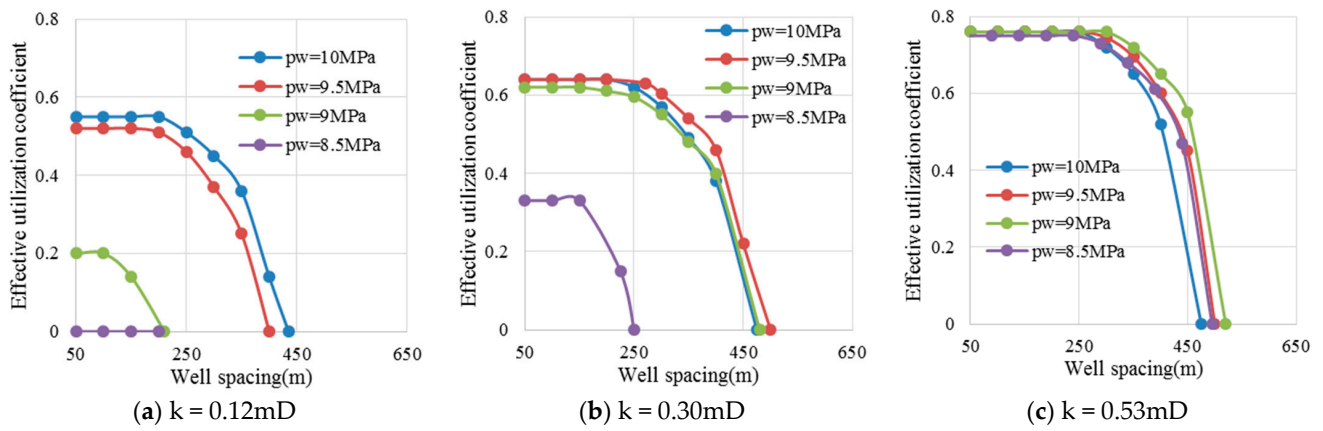
Figure 21. The relationship between the effective utilization coefficient and the well spacing after fracturing.

3.3.3. The Impact of Row Spacing

As can be seen from Figures 22 and 23, after degassing, the production rate and the effective utilization coefficient decrease as the production well pressure decreases. When the permeability is high, the decrease is smaller; and when the permeability is low, the decrease is greater. After degassing, the effective utilization factor decreases earlier and the available row spacing decreases.
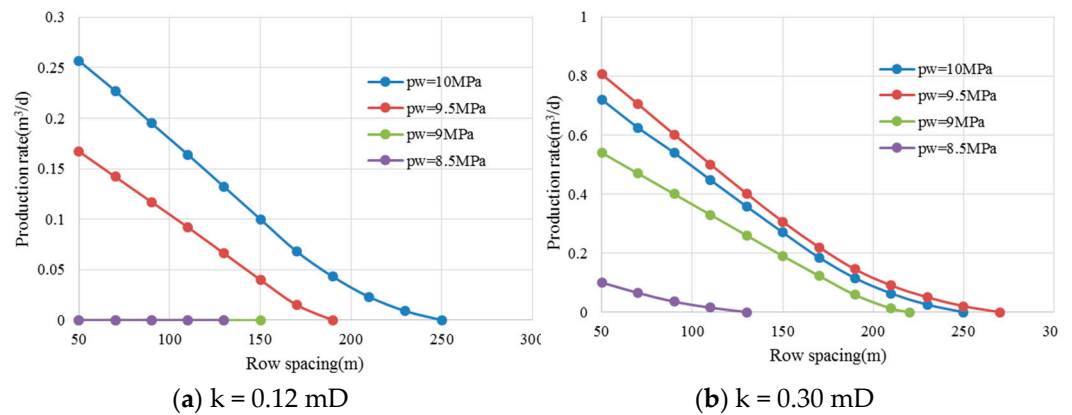
Figure 22. The relationship between the production rate and the row spacing.
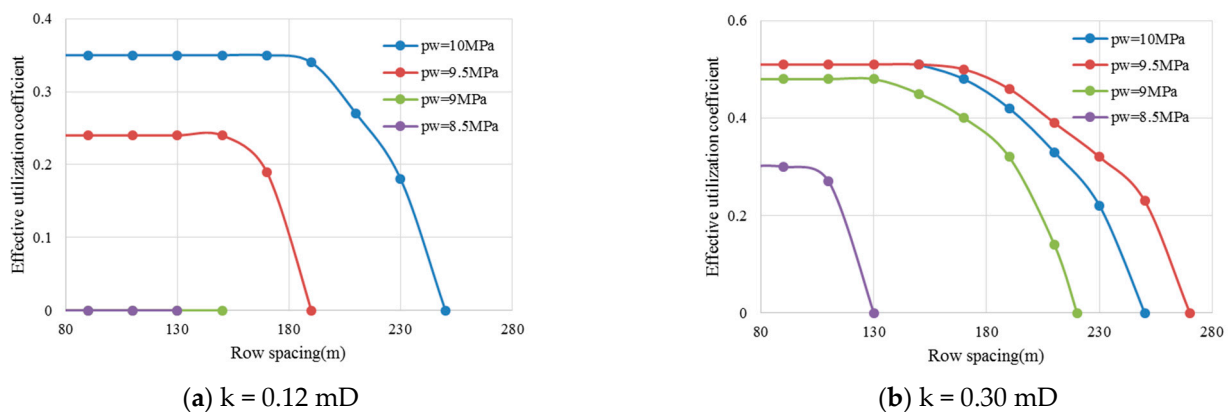
Figure 23. The relationship between the effective utilization coefficient and the row spacing.

4. Conclusions

(1) In this study, a method for determining the porous flow resistance gradient of the gas-bearing tight oil reservoirs was established. The test result curves show that when back pressure is lower than the pseudo-bubble point pressure, the solution gas begins to separate out and there is a plateau in the curves with a relatively small resistance gradient. As the back pressure decreases further, a large amount of solution gas separates out and forms a continuous gas phase, causing the resistance gradient to increase rapidly and exponentially.

(2) The concept of the pseudo-bubble point pressure was proposed. The lower the permeability, the higher the pseudo-bubble point pressure. The lower the permeability, the greater the resistance gradient under the same back pressure.

(3) For tight reservoirs, when the permeability is less than 0.3 mD, the production pressure should be maintained above the pseudo-bubble point pressure (about 10% below the bubble point pressure). When the permeability is greater than 0.3 mD, the production pressure can be lowered to below the pseudo-bubble point pressure (about 15% below the bubble point pressure).

(4) A mathematical model of porous flow in a rectangular injection–production well network in a gas-bearing tight oil reservoir was established. The streamline integration method was used, and the threshold pressure gradient and the additional resistance generated by the separated gas were considered. The oil production rate and the effective utilization coefficient were calculated.

(5) After degassing, the oil production rate and the effective utilization coefficient of the oil wells decrease rapidly. The formation with the higher permeability decreases later and has a flat trend, and the production well pressure can be reduced to a lower level.

(6) Fracturing can effectively increase the oil production rate after degassing. A formation that cannot be utilized before fracturing because of the throats are blocked by the separated solution gas can also produce some oil. When the production well pressure is lower than the bubble point pressure, which is not too large, the fracturing effect is better.

Author Contributions: Writing—original draft preparation, Y.R.; resources, Z.Y.; funding acquisition, Y.Z.; methodology, Y.H.; software, Z.W.; investigation, Y.L.; formal analysis, H.L. All authors have read and agreed to the published version of the manuscript.

Institutional Review Board Statement: Not applicable.

Informed Consent Statement: Not applicable.

Data Availability Statement: The data presented in this study are available in this article.

Conflicts of Interest: The authors declare no conflict of interest.

References

1. Hu, S.Y.; Tao, S.Z.; Yan, W.P.; Men, G.T.; Tang, Z.X.; Xue, J.Q.; Jia, X.Y. Advances on continental tight oil accumulation and key technologies for exploration and development in China. *Nat. Gas Geosci.* **2019**, *30*, 1083–1093.
2. Kang, Y.Z. Resource potential of tight sand oil & gas and exploration orientation in China. *Nat. Gas Ind.* **2016**, *36*, 10–18.
3. Zou, C.N.; Yang, Z.; Zhu, R.K.; Zhang, G.S.; Hou, L.H.; Wu, S.T.; Tao, S.Z. Progress in China's unconventional oil & gas exploration and development and theoretical technologies. *Acta Geol. Sin.* **2015**, *89*, 979–1007.
4. Hassanpouryouzband, A.; Joonaki, E.; Farahani, M.V.; Takeya, S.; Ruppel, C.; Yang, J.; English, N.J.; Schicks, J.M.; Edlmann, K.; Mehrabian, H.; et al. Gas hydrates in sustainable chemistry. *Chem. Soc. Rev.* **2020**, *49*, 5225–5309. [CrossRef] [PubMed]
5. Yang, J.; Hassanpouryouzband, A.; Tohidi, B.; Chuvilin, E.; Bukhanov, B.; Istomin, V.; Cheremisin, A. Gas Hydrates in Permafrost: Distinctive Effect of Gas Hydrates and Ice on the Geomechanical Properties of Simulated Hydrate-Bearing Permafrost Sediments. *J. Geophys. Res. Solid Earth* **2019**, *124*, 2551–2563. [CrossRef]
6. Fang, X.; Yang, Z.; Guo, X.G.; Wu, Y.X.; Liu, J.T. Resource grading evaluation and exploration potential of tight oil in major basins of China. *Gas Sci. Geosci.* **2019**, *30*, 1094–1105.
7. Zhu, X.M.; Pan, R.; Zhu, S.F.; Wei, W.; Ye, L. Research progress and core issues in tight reservoir exploration. *Earth Sci. Front.* **2018**, *25*, 141–146.

8. Du, J.H.; He, H.Q.; Yang, T.; Li, J.Z.; Huang, F.X.; Guo, B.C.; Yan, W.P. Progress in China's tight oil exploration and challenges. *China Pet. Explor.* **2014**, *19*, 1–9.

9. Zou, C.N.; Zhu, R.K.; Wu, S.T.; Yang, Z.; Tao, S.Z.; Yuan, X.J.; Hou, L.H. Types, characteristics, genesis and prospects of conventional and unconventional hydrocarbon accumulations: Taking tight oil and tight gas in China as an instance. *Acta Pet. Sin.* **2012**, *33*, 173–187.

10. Al-Hosani, A.; Ravichandran, S.; Daraboina, N. Review of Asphaltene Deposition Modeling in Oil and Gas Production. *Energy Fuels* **2021**, *35*, 965–986. [CrossRef]

11. Lin, Y.; Cao, T.; Chacón-Patiño, M.L.; Rowland, S.M.; Rodgers, R.P.; Yen, A.; Biswal, S.L. Microfluidic Study of the Deposition Dynamics of Asphaltene Subfractions Enriched with Island and Archipelago Motifs. *Energy Fuels* **2019**, *32*, 1882–1891. [CrossRef]

12. Hassanpouryouzband, A.; Joonaki, E.; Taghikhani, V.; Boozarjomehry, R.B.; Chapoy, A.; Tohidi, B. New Two-Dimensional Particle-Scale Model to Simulate Asphaltene Deposition in Wellbores and Pipelines. *Energy Fuels* **2018**, *32*, 2661–2672. [CrossRef]

13. Hu, S.Y.; Zhu, R.K.; Wu, S.T.; Bai, B.; Yang, Z.; Cui, J.W. Profitable exploration and development of continental tight oil in China. *Pet. Explor. Dev.* **2018**, *45*, 737–748. [CrossRef]

14. Xiao, Q.H. The Reservoir Evaluation and Porous Flow Mechanism for Typical Tight Oilfields. Ph.D. Thesis, University of Chinese Academy of Sciences, Beijing, China, 2015.

15. Du, J.H.; Liu, H.; Ma, D.S.; Wang, Y.H.; Zhou, T.Y. Discussion on effective development techniques for continental tight oil in China. *Pet. Explor. Dev.* **2014**, *41*, 198–205. [CrossRef]

16. Wei, Y.Y. Study on Tight Sandstone Reservoir Characteristics and Development in Sichuan. Ph.D. Thesis, University of Chinese Academy of Sciences, Beijing, China, 2017.

17. Xiao, Q.H.; Wang, Z.Y.; Yang, Z.M.; Liu, X.W.; Wei, Y.Y. Porous flow characteristics of solution-gas drive in tight oil reservoirs. *Open Phys.* **2018**, *16*, 412–418.

18. Akin, S.; Kovscek, A.R. Heavy-oil solution gas drive: A laboratory study. *J. Pet. Sci. Eng.* **2002**, *35*, 33–48. [CrossRef]

19. Chen, X.L.; Qing, J.S. Visualization study on foamy oil flow state. *J. Southwest Pet. Univ.* **2009**, *31*, 126–130.

20. Chen, Z.X.; Sun, J.; Wang, R.H.; Xiao, D.W. A pseudobubblepoint model and its simulation for foamy oil in porous media. *SPE J.* **2015**, *20*, 239–247. [CrossRef]

21. George, D.S.; Hayat, O.; Kovscek, A.R. A microvisual study of solution-gas-drive mechanisms in viscous oils. *J. Pet. Sci. Eng.* **2005**, *46*, 101–119. [CrossRef]

22. Li, S.Y.; Li, Z.M.; Wang, Z.Z. Experimental study on the performance of foamy oil flow under different solution gas-oil ratios. *RSC Adv.* **2015**, *5*, 66797–66806. [CrossRef]

23. Lu, T.; Li, Z.M.; Li, S.Y.; Li, X.M.; Wang, P.; Wang, Z.Z. Physical and numerical simulations of flow characteristics in solution gas drive for heavy oils. *Acta Pet. Sin.* **2014**, *35*, 332–339.

24. Cui, G.L.; Zhang, Y.Y.; Sun, X.F.; Duan, X.W. Foamy oil characteristics of dissolved gas drive in heavy crude. *Complex Hydrocarb. Reserv.* **2013**, *6*, 55–58.

25. Liu, P.C.; Wu, Y.B.; Li, X.L. Experimental study on the stability of the foamy oil in developing heavy oil reservoirs. *Fuel* **2013**, *111*, 12–19. [CrossRef]

26. Lu, T.; Li, Z.M.; Li, S.Y.; Li, B.F.; Liu, S.Q. Performances of different recovery methods for Orinoco Belt heavy oil after solution gas drive. *Energy Fuels* **2013**, *27*, 3499–3507. [CrossRef]

27. Ostos, A.T.; Maini, B.B. An integrated experimental study of foamy oil flow during solution gas drive. *J. Can. Pet. Technol.* **2005**, *44*, 43–50. [CrossRef]

28. Turta, A.T.; Maini, B.B.; Jackson, C. Mobility of gas-in-oil dispersions in enhanced solution gas drive (foamy oil) exploitation of heavy oil reservoirs. *J. Can. Pet. Technol.* **2003**, *42*, 48–55. [CrossRef]

29. Sun, X.F.; Zhang, Y.Y.; Li, X.M.; Li, W.W.; Song, H.H. Simulation model evaluation in foamy oil reservoir and porous flow mechanism study based on experimental matching. *J. China Univ. Pet.* **2013**, *37*, 114–118.

30. Wang, L.; Rao, L.Y.; Li, W.; Li, J. Experimental study and numerical simulation on P oilfield in the progress of water injection. *J. Southwest Pet. Univ.* **2011**, *33*, 109–114.

31. Li, B.; Li, T.L.; Zhang, Y.C. Experimental research of water flooding time in high permeability sandstone reservoirs. *Acta Pet. Sin.* **2007**, *28*, 78–82.

32. Zhang, S.L.; Huang, Y.M.; Niu, M.C.; Zhu, K. Tracking optimum development by water injection and achieve effect in Chengdao oilfield. *J. Southwest Pet. Inst.* **2003**, *25*, 46–48.

33. Ahmadpour, M.; Siavashi, M.; Moghimi, M. Numerical simulation of two-phase mass transport in three-dimensional naturally fractured reservoirs using discrete streamlines. *Numer. Heat Transf. Part A Appl.* **2018**, *73*, 482–500. [CrossRef]

34. Wang, S.R.; Cheng, L.S.; Huang, S.J.; Xue, Y.C.; Bai, M.H.; Wu, Y.H.; Jia, P. A Semi-Analytical Method for Modeling Two-Phase Flow Behavior in Fractured Carbonate Oil Reservoirs. *J. Energy Resour. Technol.* **2019**, *141*, 072902. [CrossRef]

35. Lu, X.Q.; Zhou, X.; Luo, J.X.; Zeng, F.H.; Peng, X.L. Characterization of Foamy Oil and Gas/Oil Two-Phase Flow in Porous Media for a Heavy Oil/Methane System. *J. Energy Resour. Technol.* **2018**, *141*, 032801. [CrossRef]

36. Wang, S.R.; Cheng, L.S.; Xue, Y.C.; Huang, S.J.; Wu, Y.H.; Jia, P.; Sun, Z. A Semi-Analytical Method for Simulating Two-Phase Flow Performance of Horizontal Volatile Oil Wells in Fractured Carbonate Reservoirs. *Energies* **2018**, *11*, 2700. [CrossRef]

37. Wu, Y.H.; Cheng, L.S.; Huang, S.J.; Bai, Y.H.; Jia, P.; Wang, S.R. An approximate semianalytical method for two-phase flow analysis of liquid-rich shale gas and tight light-oil wells. *J. Pet. Sci. Eng.* **2019**, *176*, 562–572. [CrossRef]

38. Siripatrachai, N.; Ertekin, T.; Johns, R.T. Compositional Simulation of Hydraulically Fractured Tight Formation Considering the Effect of Capillary Pressure on Phase Behavior. *SPE J.* **2017**, *22*, 1046–1063. [CrossRef]

39. Qin, Y.; Yao, S.; Xiao, H.; Cao, J.; Hu, W.; Sun, L.; Tao, K.; Liu, X. Pore structure and connectivity of tight sandstone reservoirs in petroleum basins: A review and application of new methodologies to the Late Triassic Ordos Basin, China. *Mar. Pet. Geol.* **2021**, *129*, 105084. [CrossRef]

40. Wang, F.J.; Liu, Y.K.; Yu, S.H. Reservoir characteristics of tight sandstone in the eastern Sulige Gas Field. *Pet. Geol. Recovery Effic.* **2017**, *24*, 43–47.

41. Zhu, Y.C.; Jiang, Y.Y.; Wu, J.J.; Yang, S.; Guo, X.G. Quantitative prediction of tight oil reservoir properties in Jumusar depression. *Spec. Oil Gas Reserv.* **2017**, *24*, 42–47.

42. Zhao, X.L.; Yang, Z.M.; Lin, W. Study on pore structures of tight sandstone reservoirs based in nitrogen absorption, high-pressure mercury intrusion and rate-controlled mercury intrusion. *J. Energy Resour. Technol.* **2019**, *141*, 112903. [CrossRef]

43. Yang, Z.M.; Guo, H.K.; Liu, X.W. *Micro-Pore Structure Test and Physical Simulation Technology of Low Permeability-Tight Reservoirs*; Petroleum Industry Press: Beijing, China, 2017.

44. Zhang, X.L. Calculation of natural depletion oil recovery for low permeability reservoirs. *J. Liaoning Tech. Univ.* **2014**, *33*, 633–636.

45. Song, Y.L.; Song, Z.J.; Feng, D.; Qin, J.H.; Chen, Y.K.; Shi, Y.L.; Hou, J.R.; Song, K.P. Phase behavior of hydrocarbon mixture in shale nanopores considering the effect of adsorption and its induced critical shifts. *Ind. Eng. Chem. Res.* **2020**, *59*, 8374–8382. [CrossRef]

46. Zhao, Y.N.; Wang, Y.N.; Zhong, J.J.; Xu, Y.; Sinton, D.; Jin, Z.H. Bubble point pressures of hydrocarbon mixtures in multiscale volumes from density functional theory. *Langmuir* **2018**, *34*, 14058–14068. [CrossRef] [PubMed]

47. Nojabaei, B.; Johns, R.T.; Chu, L. Effect of capillary pressure on phase behavior in tight rocks and shales. *SPE Reserv. Eval. Eng.* **2013**, *16*, 281–289. [CrossRef]

48. Zhang, M.L.; Mei, H.Y.; Li, M.; Sun, L.T.; Li, S.L.; Wu, Q.S. A phase equilibrium model in volatile petroleum system under consideration of capillary pressure. *China Offshore Oil Gas* **2002**, *16*, 48–51.

49. He, Y. *Research on Reservoir Engineering Method of Low Permeability Reservoir Well Pattern Deployment*; Graduate School of Chinese Academy of Sciences, Institute of Percolation Fluid Mechanics: Langfang, China, 2009.